Relaxation Dynamics in See-Saw Shaped Dy(III) Single-Molecule Magnets

Journal:	*Inorganic Chemistry Frontiers*
Manuscript ID	QI-RES-08-2020-001007.R1
Article Type:	Research Article
Date Submitted by the Author:	22-Aug-2020
Complete List of Authors:	Murugesu, Muralee; Ottawa University, Department of Chemistry Harriman, Katie; Ottawa University, Department of Chemistry Murillo, Jesse; University of Texas at El Paso, Chemistry Suturina, Elizaveta; University of Southampton, Fortier, Skye; University of Texas at El Paso, Department of Chemistry

ARTICLE

Relaxation Dynamics in See-Saw Shaped Dy(III) Single-Molecule Magnets

Katie L. M. Harriman,[a] Jesse Murillo,[b] Elizaveta A. Suturina,[c] Skye Fortier,*[b] and Muralee Murugesu*[a]

Utilizing a terphenyl bisanilide ligand, two Dy(III) compounds $[K(DME)_n][L^{Ar}Dy(X)_2]$ ($L^{Ar} = \{C_6H_4[(2,6-^iPrC_6H_3)NC_6H_4]_2\}^{2-}$), X = Cl (**1**) and X = I (**2**) were synthesized. The ligand imposes an unusual see-saw shaped molecular geometry leading to a coordinatively unsaturated metal complex with near-linear N-Dy-N (avg. 159.9° for **1** and avg. 160.4° for **2**) angles. These compounds exhibit single-molecule magnet (SMM) behavior with significant uniaxial magnetic anisotropy as a result of the transverse coordination of the bisanilide ligand which yields high energy barriers to magnetic spin reversal of U_{eff} = 1334 K/ 927cm^{-1} (**1**) and 1278 K/ 888 cm^{-1} (**2**) in zero field. *Ab initio* calculations reveal that the dominant crystal field of the bisanilide ligand controls the orientation of the main magnetic axis which runs nearly parallel to the N-Dy-N bonds, despite the identity of the halide ligand. Analysis of the relaxation dynamics reveals a *ca.* 14-fold decrease in the rate of qunatum tunneling of the magnetisation when X = I (**2**). Most notably, the relaxation times were on average 5.6x longer at zero field when the heavier group 17 congener was employed. However, no direct evidence of a heavy atom effect on the Orbach relaxation was obtained as the height of the barrier is defined by the dominant bisanilide ligand.

Introduction

Since the discovery of domain-independent magnetism of molecular origin in 1991,[1] single-molecule magnets (SMMs) have captivated the imagination of researchers for their potential use in advanced magnetic materials and applications. In particular, these molecules exhibit a magnetic memory response, or hysteresis, where molecular magnetisation persists upon removal of the external magnetic field.[2,3] This makes SMMs potentially suitable for new high-capacity, magnetic-based data storage devices or even quantum computing.[4,5] A major drawback, however, is the magnetic blocking temperature (T_B), a figure of merit for the ability to retain magnetisation, is often limited to cryogenic temperatures typically nearing the boiling point of liquid helium. While several factors can affect T_B and SMM activity, an important parameter to overall SMM performance is the effective energy barrier to magnetic spin reversal (U_{eff}). Large U_{eff} values (> 1000 K / 695 cm^{-1}) are requisite for maintaining SMM activity at elevated temperatures.[3,6]

In this regard, recent attention has been focused on the development of lanthanide based SMMs with staggering U_{eff}.[3,6]

Traditionally, the core-like 4f-orbitals were described as insensitive to covalent ligand field contributions, which allows for significant orbital degeneracy and spin-orbit coupling that gives way to large magnetic moments. However, both electrostatic and covalent contributions to the crystal field affect the splitting of magnetic microstates, thus enhancing the magnetic anisotropy.[7–10] Based upon crystal field theory, the symmetry, point charge effects, and the relative shape of the 4f free-ion electron density should be considered when designing ligand frameworks to maximize magnetic anisotropy and consequently U_{eff} values.[6,11–13]

This strategy has recently proven effective with oblate-shaped Dy(III) in near-linear or linearly dominant crystal fields.[14–22] For instance, in $(NN^{TBS})Dy(I)(THF)_2$ (NN^{TBS} = $Fc(NHSi^tBuMe_2)_2$), the diamide ligand produces a highly axial crystal field for the Dy(III) ion with N-Dy-N = 134.7(2)°, affording a SMM with an appreciable U_{eff} = 770.8 K (535.7 cm^{-1}) / 910 K (632.5 cm^{-1}).[19,23] Although not mononuclear, in a related system, the two monodentate anilide ligands in $[Dy(N^{RR'})_2(\mu-Cl)_2K]_n$ ($N^{RR'} = \{N(SiMe_3)(C_6H_3^iPr_2-2,6)\}^-$) afford a U_{eff} = 1578 K in zero field.[24] In $[Dy(O^tBu)_2(py)_5][BPh_4]$, the *trans* oriented (O-Dy-O = 178.91(9)°) alkoxide donors and, in relation, the less donating equatorially-bound pyridine ligands give rise to a SMM with a tremendous U_{eff} = 1815 K (1261.5 cm^{-1}) and T_B = 14 K (ZFC-FC susceptibilities).[15] This was recently surpassed by $[(Cp^{iPr5})Dy(Cp^*)][B(C_6F_5)_4]$ (Cp^{iPr5} = 1,2,3,4,5-($^iPr)_5C_5$; Cp^* = 1,2,3,4,5-(Me)C_5), which fully excludes equatorial ligands to give near-linear coordinated dysprosium (Cp-Dy-Cp = 162.507(1)°). In this case, the metal complex displays a record setting U_{eff} =

2217 K (1541 cm^{-1}) and a remarkable T_B = 80 K (25 Oe s^{-1}) that exceeds the temperature of liquid nitrogen (77 K).[13]

These results clearly demonstrate a successful design criterion for enhancing magnetic anisotropy; yet, several questions remain. With respect to Dy(III), the linear deviation tolerance of the axial ligation mode is not fully established. While linear two-coordinate dysprosium has been predicted as optimal for maximizing U_{eff},[6,14] five-coordinate and seven-coordinate Dy(III) in (NN^{TBS})Dy(I)(THF)$_2$ and [Dy(O^{t}Bu)$_2$(py)$_5$][BPh$_4$], respectively, still exhibit notable magnetic anisotropy enhancements due to strong metal-ligand interactions along a defined axis, regardless of their molecular geometry or symmetry. This strong interaction and axiality enhancement define the barrier of magnetisation spin reversal, however; as energy barriers continue to rise, the through barrier mechanisms become increasingly more important to understand. Spin-vibrational coupling has been identified for facilitating these processes (i.e. Raman relaxation). Strategies to suppress vibrational coupling have been reported as ways to improve the performance of SMMs without necessarily increasing the U_{eff}.[25,26] Increasing the rigidity of ligand frameworks represents the most accessible and tunable approach for synthetic chemists.[27,28] Thus, the effects of coordination geometry, total coordination number, and the identity/ role of the ligands in processes beyond quantum tunneling of the magnetisation (QTM) have yet to be completely determined.

We recently reported the synthesis and characterisation of the U(III) compound L^{Ar}U(I)(DME) (L^{Ar} = {C$_6$H$_4$[(2,6-^{i}PrC$_6$H$_3$)NC$_6$H$_4$]$_2$}$^{2-}$) featuring a terphenyl bisanilide ligand with near-linear coordinated nitrogen atoms (N1–U1–N2 =162.8(1)°).[29] In L^{Ar}U(I)(DME), the uranium atom is tethered above a central phenyl ring, which exhibits nominal metal-arene interactions. As such, this central ring acts to block several coordination sites on the metal. Structurally, this platform provides a number of attractive features for utilisation with Dy(III) in pursuit of enhanced SMM properties. It possesses a defined orientation for the magnetic anisotropy (N1-M-N2), as well as a tethered backbone for increased ligand stiffness, combined with an X-ligand which represents a tunable position for the investigation of halide effects on the magnetic properties. Here we describe the synthesis and magnetic characterisation of two dysprosate metal complexes, [K(DME)$_3$][L^{Ar}Dy(Cl)$_2$] (**1**) and [K(DME)$_4$][L^{Ar}Dy(I)$_2$] (**2**), which each feature a Dy(III) ion with an unusual see-saw geometry and near-linear N-Dy-N arrangement. The relaxation dynamics of each system are analysed, and we attempt to address whether there is a fundamental link between the different structural features (i.e. the transverse ligand architecture and halide ancillary ligands) and the observed magnetic properties.

Results and Discussion

Synthesis and Structural Studies

Following the procedure for the synthesis of the *N,N*-chelated {[ArNCC(Me)]$_2$CH}DyCl$_2$(THF)$_2$,[30] a solution of DyCl$_3$

and [K(DME)$_2$]$_2$L^{Ar} in THF was heated at 60 °C for two days, giving a mixture from which **1** was isolated in low yield as a THF solvate. Notably, the formation of **1**·THF under this setting is accompanied by unreacted DyCl$_3$ and a significant amount of protonated H$_2$L^{Ar} despite strictly anhydrous conditions. This result suggests that **1** may become unstable at elevated temperatures. To counter this, addition of DyCl$_3$ to a thawing THF solution of [K(DME)$_2$]$_2$L^{Ar} followed by warming to room temperature and stirring for 12 h gives **1** as air and moisture sensitive crystals in 47% yield after recrystallisation from DME. Similarly, **2** was synthesized using identical conditions to those of **1**, giving 55% crystalline yield (see Scheme 1). The ^{1}H NMR spectrum of **1** in THF-d_8 reveals several paramagnetically broadened resonances spanning from -401.5 to 317.3 ppm (Fig. S1). Likewise, the ^{1}H NMR spectrum of **2** in THF-d_8 shows paramagnetic resonances from -348.6 to 328.2 ppm (Fig. S2).
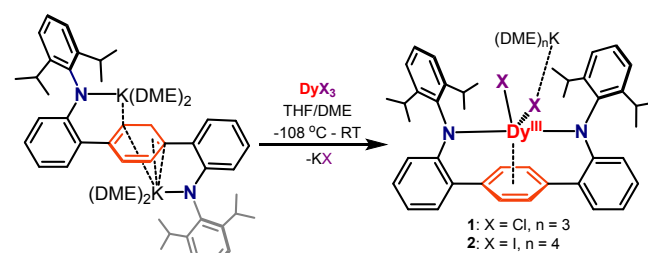
Scheme 1. Synthesis of [K(DME)$_3$][L^{Ar}Dy(Cl)$_2$] (**1**) and [K(DME)$_4$][L^{Ar}Dy(I)$_2$] (**2**).

Compound **1** crystallises at -25 °C in the monoclinic space group *Cc* (see ESI†). The X-ray diffraction analysis at 100 K reveals two independent molecules in the asymmetric unit, each exhibiting severe positional and solvent disorder. However, data collection at 15 K under a He cryostream shows a crystallographic phase transition to monoclinic *Pn* with four well-resolved molecules in the asymmetric unit (**1-Dy1**, **1-Dy2**, **1-Dy3**, **1-Dy4**; Fig. S5-S6). Comparatively, **2** crystallises at -35 °C in the triclinic space group *P*$\bar{1}$ (Fig. S7; Table S1). The dysprosium compounds of **1** and **2** are isotypic, and as a representative, the solid-state molecular structure of **1-Dy2** is shown in Fig. 1. As compared to (NN^{TBS})Dy(I)(THF)$_2$ (Dy-N = avg. 2.21 Å), [Dy(N$^{RR'}$)$_2$(μ-Cl)$_2$K]$_n$ (Dy-N = avg. 2.25 Å), and [Li(THF)$_4$][Dy(NPh$_2$)$_4$] (Dy-N = avg. 2.29 Å),[19,24,31] the Dy-N distances in **1** (2.379(9)-2.416(8) Å) and **2** (2.402(7)-2.438(8) Å) are substantially elongated. These larger Dy-N distances may be attributed to the transverse structure of the bis-anilide ligand, constraining the N-donor atoms into positions where the Dy-N distances are relatively long. Yet, the ligand bite angle in **1** (N-Dy-N = avg. 159.9°) and **2** (N-Dy-N = 160.4(2)°) is more obtuse than that of (NN^{TBS})Dy(I)(THF)$_2$ (N-Dy-N = 134.7(2)°) and [Dy(N$^{RR'}$)$_2$(μ-Cl)$_2$K]$_n$ (N-Dy-N = avg. 131.6°). Collectively, this demonstrates the inter-complementary role of the bite angle and distances in the ligand design of such metal complexes. Although the extent of the interactions between Dy and the central terphenyl ring (Dy-C$_{cent}$ = avg. 2.56 Å for **1**, and Dy-C$_{cent}$ = 2.55 Å for **2**) cannot be fully excluded from the discussion, they are assumed to be minimal due to the neutral charge of this moiety. Comparatively, the compound [((^{Ad,Me}ArO)$_3$mes)Dy]

exhibits a similar tethered arene backbone (Dy-C$_{cent.}$ = 2.368 Å),[32] further supporting the weak Dy-arene interaction in **1** and **2**. Thus, any metal-π interactions present in **1** and **2** are not strong directors of the magnetic anisotropy (*vide infra*). The remaining coordination sites on the Dy(III) ion are occupied by two halide ions, which possess distances typical for Dy-X (**1**; Dy-Cl = 2.510(3)-2.579(3) Å and **2**; Dy-I = 2.9355(7)-2.9771(5) Å).[33] Thus, the Dy(III) ion in **1** and **2** adopts an unusual see-saw type geometry because of the coordination environment enforced by the bulky, transverse ligand architecture.
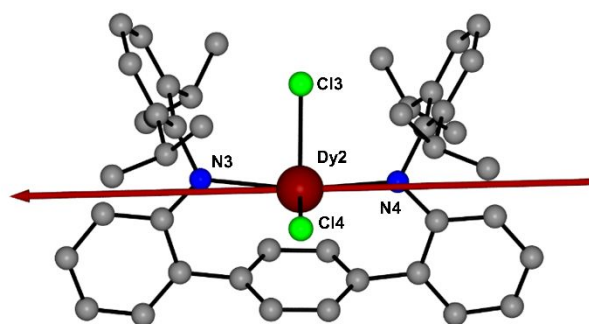

Fig. 1 Representative solid-state molecular structure of **1-Dy2** (*see Fig. S5-S7*). Protons and [K(DME)$_3$]$^+$ cation removed for clarity. Solid red vector depicts the calculated orientation of the main magnetic axis in the ground Kramers doublet of **1-Dy2**.

Theoretical Analysis

Ab initio calculations on two of the molecules in the asymmetric unit of **1** featuring the maximum (**1-Dy2**) and minimum (**1-Dy4**) N-Dy-N angles (162.7° and 156.2°, respectively) as well as the iodo-derivative (**2**) were completed with SO-CASSCF(9,7)/ANO-RCC in MOLCAS 8.0.[34] The computed eight Kramer's doublets (KDs) of $^6H_{15/2}$ span 1120 cm^{-1} (**1-Dy2**), 998 cm^{-1} (**1-Dy4**), and 1173 cm^{-1} (**2**) (Tables S2-S7). The ground KDs have large principle *g*-tensors; g'_z = 19.9567 (**1-Dy2**), 19.8300 (**1-Dy4**), and 19.883 (**2**), in which the magnetic axis is nearly collinear to the Dy-N bonds (Fig. 1). Previously, the amido N-atoms of (NN^{TBS})Dy(I)(THF)$_2$ were proven to be greater directors of magnetic anisotropy over the bound halide and solvent (THF).[19] Thus, it is not surprising that the strong electrostatic interaction of the N-atoms of the bisanilide ligand in **1** and **2** dictates the orientation of the main magnetic axis of the Dy(III) ions more strongly than the coordinated halide ions or any interactions from the central terphenyl ring. There is negligible transverse anisotropy in the ground state KDs of all the species studied, suggesting that there should be an absence of ground-state QTM. The first excited KD lies at 323 cm^{-1}, 294 cm^{-1} and 337 cm^{-1} for **1-Dy2**, **1-Dy4**, and **2** respectively. The second and third excited state KDs also have highly axial principle *g*-values, which suggests that thermally activated relaxation should occur at least through these states. Significant transverse components of the *g*-tensor are observed at the 4th KD for **1-Dy2** (g'_x = 2.7977, g'_y = 6.161, g'_z = 8.9011), **1-Dy4** (g'_x = 1.9353, g'_y = 3.4765, g'_z = 10.1002), and **2** (g'_x = 1.6501, g'_y = 1.3082, g'_z = 11.1331). Large principle *g*-tensors; g'_z = 19.0299 (**1-Dy2**), 19.0753 (**1-Dy4**), and 18.714 (**2**); are obtained once again in the 8th KD for all species. Thus, thermal relaxation is

expected to occur *via* the 4th KD for both **1** and **2** with activation energies of 1088-1204 K (**1**) and 1304 K (**2**).

As a representative example, the calculated transition matrix probabilities of compound **1-Dy2** displays minimal ground state QTM, with a transition magnetic moment of 8.2 x 10^{-5} μ$_B$ (Fig. 2). The transition magnetic moment of the 2nd KD is two orders of magnitude larger (5.1 x 10^{-3} μ$_B$) than the ground state (1st KD), which coincides with an increase in the transverse components of the *g*-tensor for the 2nd KD (g'_x = 0.0138, g'_y = 0.0165). At the 3rd KD, the transition magnetic moment is an order of magnitude larger (4.2 x 10^{-2} μ$_B$) than the previous and correlates to a proportional increase in the transverse components of the *g*-tensor (g'_x = 0.1142, g'_y = 0.1363). The vertical transition moments connecting the states of the same magnetization in increasing energy (Fig. 2, blue lines) are significantly larger than the corresponding transverse moments, promoting a multistep relaxation pathway until the 4th KD. Here, the transverse moment (1.6 μ$_B$) becomes sufficiently large enough to yield efficient thermally activated quantum tunnelling of the magnetization (TA-QTM). To confirm the anisotropy and relaxation dynamics predicted *via ab initio* methods for **1** and **2**, the magnetic properties were analysed with SQUID magnetometry.
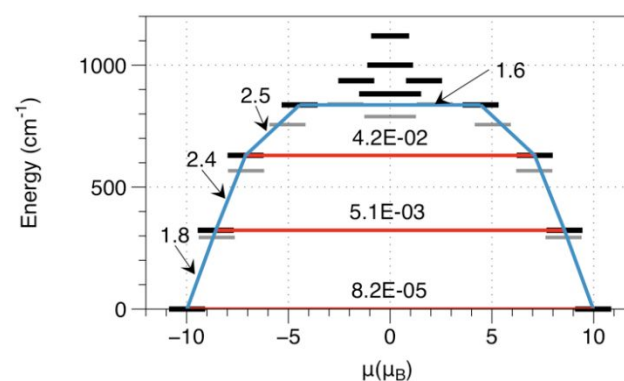

Fig. 2 Ligand field splitting of the ground term $^6H_{15/2}$ of **1-Dy2** (black bars) and **1-Dy4** (grey bars) where each KD components are spaced according to the effective magnetic projections (x-axis). Blues lines depict transitions with largest transition moments calculated with SINGLE_ANISO[35] whereas red lines depict unlikely transitions. The effective barrier for relaxation of the magnetisation due to thermally activated process is limited by the energy of the 4th KD.

Direct Current Magnetic Susceptibility Studies

The direct current (dc) magnetic susceptibility studies revealed a characteristic temperature dependence for both compounds. The near identical behaviour for **1** and **2** results in a gradual decrease in the plot of χT(T) from 13.97 cm^3·K·mol^{-1} (**1**) and 13.89 cm^3·K·mol^{-1} (**2**) at 300 K down to *ca.* 7 K suggesting strong crystal field splitting (Fig. S9). Below this temperature, a rapid decrease to final χT products of 7.92 cm^3·K·mol^{-1} (**1**) and 7.93 cm^3·K·mol^{-1} (**2**) at 1.8 K are observed. This behaviour is typical of high-performing SMMs as a result of the onset of magnetic blocking. The high temperature χT products of **1** and **2** are close to the expected value of 14.17 cm^3·K·mol^{-1} for a free Dy(III) ion ($^6H_{15/2}$, S = 5/2, L = 5, g = 4/3). The general shape of the susceptibility, in addition to the values, is in good

agreement with the ab initio calculated susceptibility which considers the local electrostatic environment of the Dy(III) ion. The field dependent magnetisation collected at 1.9, 3, 5, and 7 K for **1** and **2** exhibits sinusoidal character at low fields and reaches saturation values of 5.096 μ_B (**1**) and 5.122 μB (**2**) at 70 kOe (Fig. S10-S11). The low saturation values are indicative of an axial, well isolated ground state.[17,21,36–39]

The field-cooled (FC) and zero-field cooled (ZFC) susceptibility measurements were collected to confirm the presence of magnetic blocking as suggested by the plots of $\chi T(T)$ (Fig. S12). A clear divergence of the FC and ZFC curves occurs at 4.4 K (0.21 K min^{-1}) for both compounds, although the maximum in the ZFC susceptibilities are at 4.0 K, which is often used as a mark of T_B. Given this prospect of magnetic blocking, the magnetic hysteresis properties of **1** and **2** were measured. A mean field sweep rate of 13.6 and 12.2 Oe s^{-1}, was used for **1** and **2**, respectively (Fig. S14). Under these conditions, nearly identical waist-restricted $M(H)$ hysteresis loops were observed from 1.8-5.8 K for **1** (Fig. 3) and **2** (Fig. S13). At 1.8 K, the $M(H)$ loops are open when $H \neq 0$ Oe, with a maximum coercive field of 3687.2 Oe for **1** and 3274.5 Oe for **2** (Fig. S14). When nearing 0 Oe, the magnetisation experiences a drastic decrease with no retention of the magnetic moment, indicative of QTM. At 5.8 K, the $M(H)$ loops remain open when $H \neq 0$ Oe with a coercive field of 448.0 Oe (**1**) and 407.3 (**2**), above this temperature openings were not observable. The identical ZFC-FC susceptibilities and $M(H)$ loops of **1** and **2** suggests that the presence of a light *vs.* heavy halide has little effect on the blocking properties and the compounds ability to retain magnetisation. However; due to the variability of T_B with applied field and sweeping rate (of field or temperature), relaxation times were investigated for these compounds with the use of ac magnetic susceptibility.
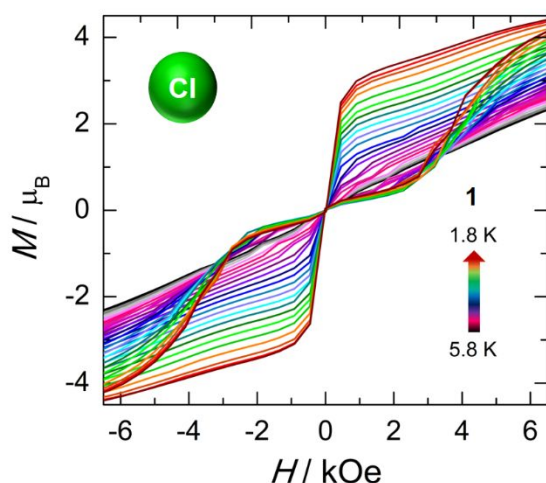

Fig. 3 Magnetic hysteresis data for **1** in the temperature range 1.8-5.8 K. Data were collected at a mean sweep rate of 13.6 Oe s^{-1}, see Fig. S13 for sweep rate vs. field plot.

Alternating Current Magnetic Susceptibility Studies

The high temperature magnetic relaxation times were probed by ac magnetic susceptibility measurements in the temperature range of 1.9-70 K for **1** and 7-62 K for **2**. using a driving field of H_{ac} = 3.78 Oe and H_{dc} = 0 Oe. The in-phase, $\chi'(v)$, (Fig. S15) and out-of-phase, $\chi''(v)$, (Fig. 4c and S16) susceptibilities as a function of ac frequency (v) for **1** display prominent SMM behaviour, with frequency dependent behaviour observable below 70 K. Below 15 K, there is little frequency dependence on χ''. Comparatively, in the $\chi'(v)$ (Fig. S18) and $\chi''(v)$ (Fig. 4d) susceptibilities for **2**, a signal was observed at a marginally smaller temperature of 62 K and persists as a frequency dependent signal until 8 K. It should be noted that the loss of frequency dependence behaviour occurs at a lower frequency for **2** than **1** (0.8 Hz *vs.* 8 Hz), suggesting that QTM effects in **1** are greater. The magnetisation relaxation times (τ) were extracted by fitting the individual $\chi'(v)$ and $\chi''(v)$ isothermal curves to the generalized Debye model (Table S8-S9; for **1**, Table S10-S11; for **2**).[40,41] Across the entirety of the temperature range studied, a minimal distribution of the relaxation times was obtained for **1**, $\alpha_{\chi'}$ = 0-0.256 and $\alpha_{\chi''}$ = 0-0.286 (Fig. S17), as well as for **2**, $\alpha_{\chi'}$ = 0.015-0.460 and $\alpha_{\chi''}$ = 0.048-0.336.

Due to the limited frequency dependence of $\chi'(v)$ and $\chi''(v)$ at low temperatures, ac measurements were performed at a fixed temperature of 20 K and the applied static field was varied from 0-5000 Oe (Fig. 3a-b). Frequency dependent behaviour was observed between 0 and 400 Oe for **1**, above which very minute changes in the characteristic frequency were observed. Similarly, **2** displayed frequency dependent behaviour between 0 and 1000 Oe; however, the deviation in peak maxima occurred over a much more narrow frequency range (2-5 Hz *vs.* 2-14 Hz). A local minimum in the characteristic frequency was obtained at 600 and 1200 Oe for **1** and **2**, respectively (Fig. S19). At these fields, QTM effects are minimized yielding longer relaxation times. The field dependent relaxation times were obtained *via* the generalized Debye model (Table S12-S13) and reveal a 6-fold increase in the relaxation time upon application of a static field for **1**. The short relaxation time of τ = 12 ms, when H_{dc} = 0 Oe, increases to τ = 72 ms at 600 Oe; comparatively, the optimal field of 1200 Oe for **2** results in a relaxation time of 84 ms, a 2.5x increase from the zero-field time (τ = 34 ms). This relaxation time is longer than the relaxation time obtained under the optimal static field for the chloro-derivative, despite the need for a larger applied static field. In fact, across the entirety of the studied field range, the iodo-derivative, **2**, exhibits longer relaxation times compared to **1** (Fig. S19).

With the goal of increasing the SMM performance of both **1** and **2** by limiting the zero-field QTM, ac susceptibility studies were completed at their respective optimal fields, 600 Oe for **1** and 1200 Oe for **2**. The effects of intermolecular interactions should also be negligible, as a field of 400 Oe or greater is necessary to decouple the dipolar interaction between nearest neighbours in the crystal lattice (Fig. S8). Under these conditions, **1** exhibited frequency dependent behaviour of the $\chi'(v)$ (Fig. S20) and $\chi''(v)$ (Fig. 4e) susceptibilities throughout the entirety of the measured temperature range (10-70 K).
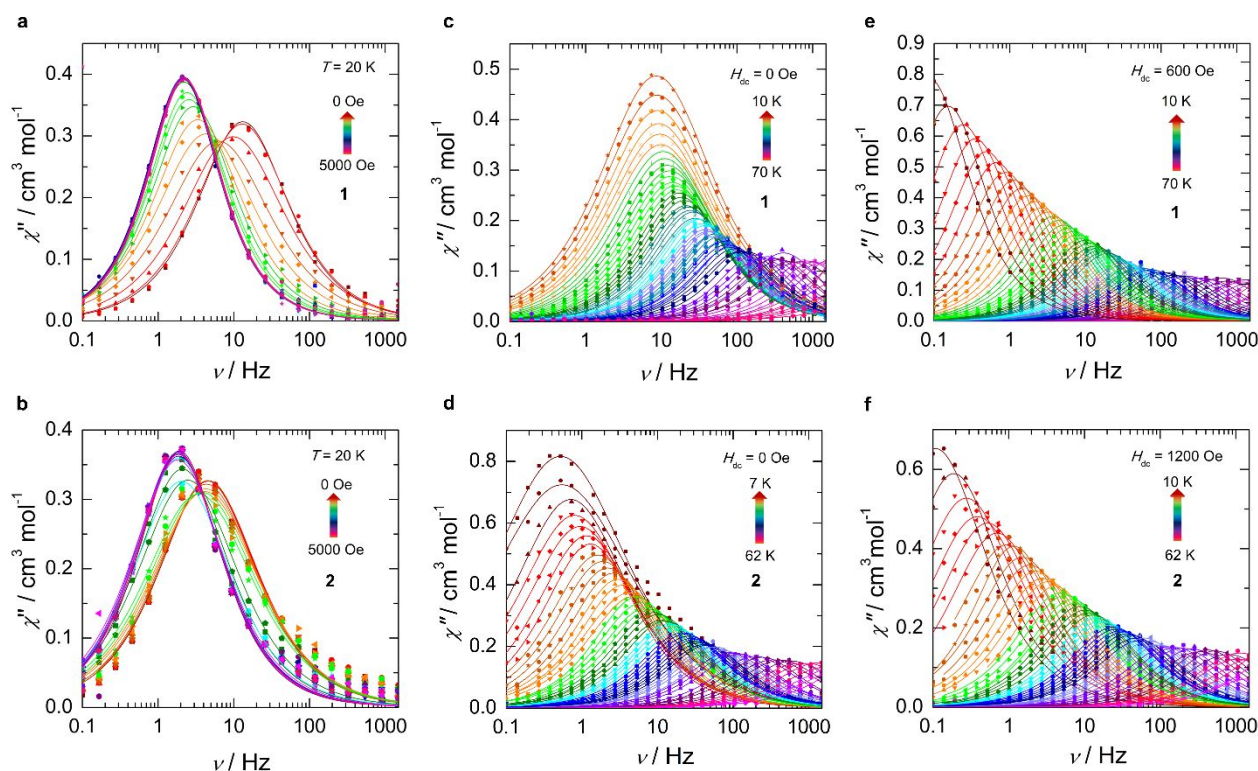
Fig. 4 (a-b) Frequency dependence of the out-of-phase (χ'') AC susceptibility as a function of applied static field at 20 K for (a) compound **1** and (b) compound **2**. (c-f) Frequency dependence of the out-of-phase (χ'') AC susceptibility at the indicated temperatures in the absence of an applied static field (H_{dc} = 0 Oe) for (c) **1** and (d) **2**, and at the optimal static field of H_{dc} = 600 for (e) **1** and H_{dc} = 1200 Oe for (f) **2**.

The τ-values were obtained from the fits of the $\chi'(\nu)$ and $\chi''(\nu)$ isotherms to the generalized Debye model (Table S14-S15),[14] which produced $\alpha_{\chi'}$ = 0-0.0745 and $\alpha_{\chi''}$ = 0-0.0561, indicating a very narrow distribution of the relaxation times (Fig. S21). With respect to **2**, upon application of a static field of 1200 Oe, frequency dependent behaviour was observed from 10-62 K in the $\chi'(\nu)$ (Fig. S22) and $\chi''(\nu)$ (Fig. 4f) susceptibilities. Below 10 K, a maximum was not observed in the $\chi''(\nu)$ plot. A narrow distribution of relaxation times was also found for this data set ($\alpha_{\chi'}$ = 0-0.371 and $\alpha_{\chi''}$ = 0-0.264; Table S16-S17).

Insight into the magnetic relaxation dynamics was obtained through the analysis and fitting of the τ vs. T^{-1} plots of **1** and **2** (Fig. 5; see Fig. S23 and S24 for τ^{-1} vs. T). Commonly, relaxation in SMMs is described by QTM, Orbach, and Raman mechanisms (Eqn. 1-2). Each of these processes possess unique temperature and field dependences which allow for the interpretation of the relaxation dynamics of each SMM. To account for these different relaxation regimes, the temperature dependent relaxation times were fit for QTM, Orbach, and Raman relaxations.

$$\tau^{-1} = \tau_{QTM}^{-1} + \tau_{Orbach}^{-1} + \tau_{Raman}^{-1} \qquad (1)$$

$$\tau^{-1} = \tau_{QTM}^{-1} + \tau_0^{-1}\exp\left(-\frac{U_{\text{eff}}}{k_B T}\right) + CT^n \qquad (2)$$

These five parameters effectively reproduce the experimental relaxation times over their respective temperature domains. For compounds **1** and **2**, the Orbach relaxation is dominate above ca. 48 K, the Raman is active between ca. 10-48 K, and only at H_{dc} = 0 Oe is QTM observed below ca. 10 K. The best fit parameters are summarized in Table S18.

The fit of the relaxation dynamics reveals large spin reversal barriers in zero field, U_{eff} = 1334 K/927 cm^{-1} (**1**) and 1278 K/888 cm^{-1} (**2**), with attempt times (τ_0) in the range 10^{-11}–10^{-15} s, as is for other high-U_{eff} SMMs (> 1000 K/ 695 cm^{-1}).[13,15,16,18,42] The lack of change in the energy barrier despite the difference in halide ion bound to the Dy(III) ion is likely a consequence of the halide not being situated along the anisotropy axis; instead the transverse bisanilide ligand dictates the height of the barrier. To support this, there is little change in the energy barriers with application of the respective optimal static fields as this process is a function of the crystal field splitting manifold. For compounds **1** and **2**, the U_{eff} values are in good agreement with the prediction from the ab initio results, that magnetic relaxation would occur via the 4th KD (ca. 900 cm^{-1}).

With respect to Raman relaxation, the C and n parameters remain relatively constant for **1** (C = 3.01 x 10^{-3}s^{-1}K^{-n}; n = 3.0) and **2** (C = 9.89 x 10^{-4}s^{-1}K^{-n}; n = 3.35) at zero field. Despite the similar parameters, the relaxation times for this regime are longer for **2**. In fact, at zero field, and 30 K, the relaxation time is more than twice (2.62 x) as long for **2** (0.011s s) compared to **1** (0.006 s).

While at their respective optimal fields, the discrepancy in the Raman relaxation times at this temperature is negligible ($\tau \approx$ 0.016 s). At the higher temperature limit of this relaxation process, there are only minor differences in the relaxation times for **1** and **2**. This may be indicative of contributions from the Orbach relaxation as the two compounds have very similar crystal field splittings (*vide supra*).
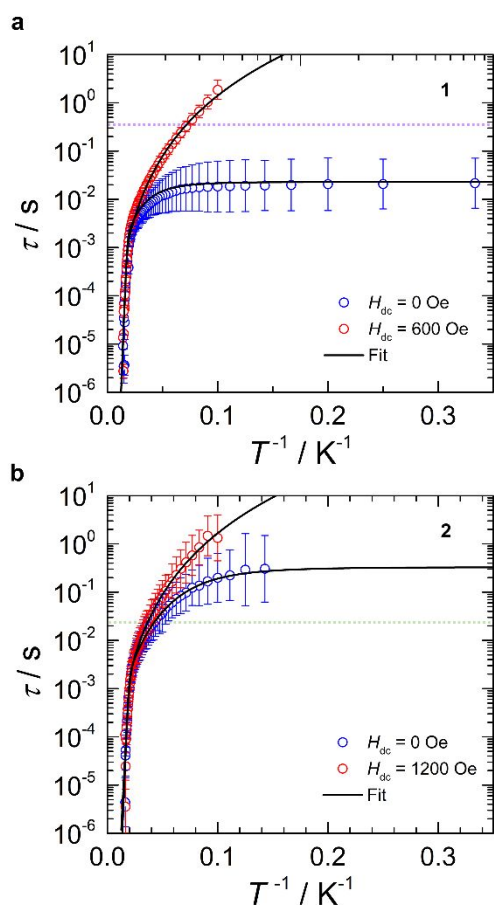

Fig. 5 (a)Temperature dependence of the magnetic relaxation times (τ) when H_{dc} = 0 Oe (circles) and H_{dc} = 600 Oe (squares) for compound **1**. Solid lines represent best-fits to Eqn. 2. The estimated standard deviations of the relaxation time have been calculated from the α-parameters of the generalised Debye fits. (b) The corresponding data for compound **2**. The dashed lines represent the QTM rates for compound **1** (green) and **2** (purple), demonstrating a faster QTM rate for **1**.

Lastly, at zero-field, the relaxation dynamics of **1** and **2** at low temperature are characterized by a QTM rate on the order of milliseconds. In the absence of an applied static field, **2** has notably less contributions from tunnelling pathways compared to **1**. The rate of tunnelling is considerably slower in the iodo-derivative compared to the rate of **1** (43.48 s^{-1} *vs.* 3.03 s^{-1}). This represents a decrease in the efficiency of the QTM process by a factor of 14 for **2**. To illustrate this significant difference, the QTM rate of **1** (green) and **2** (purple) have been represented as dotted lines on the opposing τ *vs.T* $^{-1}$ plots (Fig. 5). This means the tunnelling mechanism is more efficient and faster in the chloro-derivative which may be a consequence of the shorter Dy-X distance of **1** (2.510(3)-2.579(3) Å) *vs.* **2** (2.9355(7)-2.9771(5) Å), resulting in marginally larger transverse

components (g'_x, g'_y) of the anisotropy for **1** (*vide supra*). Nonetheless, it is evident that varying the halide ions results in notable changes in the rate of the through barrier relaxations.

Conclusions

In conclusion, the bisanilide terphenyl ligand [L^{Ar}]$^{2-}$, when coordinated to Dy(III), gives rise to an usual, see-saw shaped metal ion geometry. The transverse coordination mode of the ligand, combined with the free-ion oblate-shaped electron density of Dy(III), leads to two SMMs with impressive energy barriers to spin reversal U_{eff} = 1334 K (927cm^{-1}) and 1299 K (903 cm^{-1}) in zero field. The crystal field imposed by the bisanilide ligand is the most dominant influence on the crystal field regardless of the ancillary halide (Cl *vs.* I), thus it defines the height of the energy barrier. However; it is clear that the presence of a heavy halide leads to longer relaxation times on average, resulting in a 564% increase in zero field. While it has been proposed that the weaker more diffuse interaction of the iodide ligand would lead to overall greater SMM performance, the direct effects of this are not indicated by the U_{eff}, instead small changes to relaxation dynamics are observed. Most notably, a 14x increase in the efficiency of the QTM pathway is observed when chloride ions are bound to the Dy(III) ion. When dominant, the Raman relaxation pathway is more than twice (2.62x) as fast in the chloride (**1**) analogue *vs.* the iodide (**2**) Thus, incorporating heavier atoms into high-performing Dy^{III} SMMs is an effective way to increase the relaxation times of through barrier relaxation pathways, which would ultimately allow the Orbach process to preside over a wider temperature regime. Yet, their incorporation will not necessarily improve the U_{eff} or the blocking capabilities of a SMM, as the relative location of the heavy atoms with respect to the anisotropy axis combined with the other contributors to the crystal field are all vital to defining these features.

Conflicts of interest

There are no conflicts to declare.

Acknowledgements

Notes and references

1 R. Sessoll, D. Gatteschi, A. Caneschi and M. A. Novak, Magnetic bistability in a metal-ion cluster, *Nature*, 1993, **365**, 141–143.

2 M. Feng and M.-L. Tong, Single ion magnets from 3d to 5f: developments and strategies, *Chem. - Eur. J.*, 2018, **24**, 7574–7594.

3 D. N. Woodruff, R. E. P. Winpenny and R. A. Layfield, Lanthanide single-molecule magents, *Chem. Rev.*, 2013, **113**, 5110–5148.

4 D. Gatteschi, R. Sessoli and J. Villain, *Molecular Nanomagnets*, Oxford University Press, Oxford, 2006.

5 M. N. Leuenberger and D. Loss, Quantum computing in molecular magnets, *Nature*, 2001, **410**, 789–793.

6 N. F. Chilton, Design criteria for high-temperature single-molecule magnets, *Inorg. Chem.*, 2015, **54**, 2097–2099.

7 J. D. Rinehart and J. R. Long, Exploiting single-ion anisotropy in the design of single-molecule magnets, *Chem. Sci.*, 2011, **2**, 2078.

8 M. Briganti, G. F. Garcia, J. Jung, R. Sessoli, B. Le Guennic and F. Totti, Covalency and magnetic anisotropy in lanthanide single molecule magnets: the DyDOTA archetype, *Chem. Sci.*, 2019, **10**, 7233–7245.

9 J. Jung, M. A. Islam, V. L. Pecoraro, T. Mallah, C. Berthon and H. Bolvin, Derivation of lanthanide series crystal field parameters from first principles, *Chem. – Eur. J.*, 2019, **25**, 15112–15122.

10 L. Ungur and L. F. Chibotaru, Ab initio crystal field for lanthanides, *Chem. - Eur. J.*, 2017, **23**, 3708–3718.

11 N. F. Chilton, D. Collison, E. J. L. McInnes, R. E. P. Winpenny and A. Soncini, An electrostatic model for the determination of magnetic anisotropy in dysprosium complexes, *Nat. Commun.*, 2013, **4**, 2551.

12 N. F. Chilton, S. K. Langley, B. Moubaraki, A. Soncini, S. R. Batten and K. S. Murray, Single molecule magnetism in a family of mononuclear β-diketonate lanthanide(iii) complexes: rationalization of magnetic anisotropy in complexes of low symmetry, *Chem. Sci.*, 2013, **4**, 1719–1730.

13 F.-S. Guo, B. M. Day, Y.-C. Chen, M.-L. Tong, A. Mansikkamäki and R. A. Layfield, Magnetic hysteresis up to 80 kelvin in a dysprosium metallocene single-molecule magnet, *Science*, 2018, **362**, 1400–1403.

14 N. F. Chilton, C. A. P. Goodwin, D. P. Mills and R. E. P. Winpenny, The first near-linear bis(amide) f-block complex: a blueprint for a high temperature single molecule magnet, *Chem. Commun.*, 2015, **51**, 101–103.

15 Y.-S. Ding, N. F. Chilton, R. E. P. Winpenny and Y.-Z. Zheng, On approaching the limit of molecule magnetic anisotropy: a near-perfect pentagonal bipyramidal dysprosium(III) single-molecule magnet, *Angew. Chem. Int. Ed.*, 2016, **55**, 16071–16074.

16 C. A. P. Goodwin, F. Ortu, D. Reta, N. F. Chilton and D. P. Mills, Molecular magnetic hysteresis at 60 kelvin in dysprosocenium, *Nature*, 2017, **548**, 439–442.

17 M. Gregson, N. F. Chilton, A.-M. Ariciu, F. Tuna, I. F. Crowe, W. Lewis, A. J. Blake, D. Collison, E. J. L. McInnes, R. E. P. Winpenny and S. T. Liddle, A monometallic lanthanide bis(methanediide) single molecule magnet with a large energy barrier and complex spin relaxation behaviour, *Chem. Sci.*, 2016, **7**, 155–165.

18 F.-S. Guo, B. M. Day, Y.-C. Chen, M.-L. Tong, A. Mansikkamäki and R. A. Layfield, A dysprosium metallocene single-molecule magnet functioning at the axial limit, *Angew. Chem. Int. Ed.*, 2017, **56**, 11445–11449.

19 K. L. M. Harriman, J. L. Brosmer, L. Ungur, P. L. Diaconescu and M. Murugesu, Pursuit of record breaking energy barriers: a study of magnetic axiality in diamide ligated Dy^{III} single-molecule magnets, *J. Am. Chem. Soc.*, 2017, **139**, 1420–1423.

20 A. F. R. Kilpatrick, F.-S. Guo, B. M. Day, A. Mansikkamäki, R. A. Layfield and F. G. N. Cloke, Single-molecule magnet properties of a monometallic dysprosium pentalene complex, *Chem. Commun.*, 2018, **54**, 7085–7088.

21 Y.-S. Meng, L. Xu, J. Xiong, Q. Yuan, T. Liu, B.-W. Wang and S. Gao, Low-coordinate single-ion magnets by intercalation of lanthanides into a phenol matrix, *Angew. Chem. Int. Ed.*, 2018, **57**, 4673–4676.

22 L. Norel, L. E. Darago, B. Le Guennic, K. Chakarawet, M. I. Gonzalez, J. H. Olshansky, S. Rigaut and J. R. Long, A terminal fluoride ligand generates axial magnetic anisotropy in dysprosium complexes, *Angew. Chem. Int. Ed.*, 2018, **57**, 1933–1938.

23 M. J. Giansiracusa, A. K. Kostopoulos, D. Collison, R. E. P. Winpenny and N. F. Chilton, Correlating blocking temperatures with relaxation mechanisms in monometallic single-molecule magnets with high energy barriers (U_{eff} > 600 K), *Chem. Commun.*, 2019, **55**, 7025-7028.

24 C. Wang, R. Sun, Y. Chen, B.-W. Wang, Z.-M. Wang and S. Gao, Assembling high-temperature single-molecule magnets with low-coordinate bis(amido) dysprosium unit [DyN$_2$]$^+$ via Cl-K-Cl linkage, *CCS Chem.*, 2020, **2**, 362–368.

25 G. A. Craig, A. Sarkar, C. H. Woodall, M. A. Hay, K. E. R. Marriott, K. V. Kamenev, S. A. Moggach, E. K. Brechin, S. Parsons, G. Rajaraman and M. Murrie, Probing the origin of the giant magnetic anisotropy in trigonal bipyramidal Ni(ii) under high pressure, *Chem. Sci.*, 2018, **9**, 1551–1559.

26 M. S. Norre, C. Gao, S. Dey, S. K. Gupta, A. Borah, R. Murugavel, G. Rajaraman and J. Overgaard, High-pressure crystallographic and magnetic studies of pseudo D_{5h} symmetric Dy(III) and Ho(III) single-molecule magnets, *Inorg. Chem.*, 2020, **59**, 717–729.

27 L. Escalera-Moreno, N. Suaud, A. Gaita-Ariño and E. Coronado, Determining key local vibrations in the relaxation of molecular spin qubits and single-molecule magnets, *J. Phys. Chem. Lett.*, 2017, **8**, 1695–1700.

28 A. Castro-Alvarez, Y. Gil, L. Llanos and D. Aravena, High performance single-molecule magnets, orbach or raman relaxation suppression? *Inorg. Chem. Front.*, 2020, **7**, 2478-2486.

29 S. Fortier, J. R. Aguilar-Calderón, B. Vlaisavljevich, A. J. Metta-Magaña, A. G. Goos and C. E. Botez, An *N*-tethered uranium(III) arene complex and the synthesis of an supported U-Fe bond, *Organometallics*, 2017, **36**, 4591–4599.

30 S. V. Klementyeva, M. Yu. Afonin, A. S. Bogomyakov, M. T. Gamer, P. W. Roesky and S. N. Konchenko, Mono- and dinuclear rare-earth chlorides ligated by a mesityl-substituted β-diketiminate, *Eur. J. Inorg. Chem.*, 2016, **2016**, 3666–3672.

31 K.-X. Yu, Y.-S. Ding, T. Han, J.-D. Leng and Y.-Z. Zheng, Magnetic relaxation in four-coordinate Dy(iii) complexes: effects of anionic surroundings and short Dy-O bonds, *Inorg. Chem. Front.*, 2016, **3**, 1028–1034.

32 M. E. Fieser, C. T. Palumbo, H. S. La Pierre, D. P. Halter, V. K. Voora, J. W. Ziller, F. Furche, K. Meyer and W. J. Evans, Comparisons of lanthanide/actinide +2 ions in a tris(aryloxide)arene coordination enviornment, *Chem Sci*, 2017, **8**, 7424–7433.

33 V. S. Parmar, F. Ortu, X. Ma, N. F. Chilton, R. Clérac, D. P. Mills and R. E. P. Winpenny, Probing relaxation dynamics in five-coordinate dysprosium single-molecule magnets, *Chem. – Eur. J.*, 2020, **26**, 7774–7778.

34 F. Aquilante, J. Autschbach, R. K. Carlson, L. F. Chibotaru, M. G. Delcey, L. D. Vico, I. F. Galván, N. Ferré, L. M. Frutos, L. Gagliardi, M. Garavelli, A. Giussani, C. E. Hoyer, G. L. Manni, H. Lischka, D. Ma, P. Å. Malmqvist, T. Müller, A. Nenov, M. Olivucci, T. B. Pedersen, D. Peng, F. Plasser, B. Pritchard, M. Reiher, I. Rivalta, I. Schapiro, J. Segarra-Martí, M. Stenrup, D. G. Truhlar, L. Ungur, A. Valentini, S. Vancoillie, V. Veryazov, V. P. Vysotskiy, O. Weingart, F. Zapata and

R. Lindh, Molcas 8: new capabilities for multiconfigurational quantum chemical calculations across the periodic table, *J. Comput. Chem.*, 2016, **37**, 506–541.

35 L. F. Chibotaru and L. Ungur, Ab initio calculation of anisotropic magnetic properties of complexes. I. Unique definition of pseudospin Hamiltonians and their derivation, *J. Chem. Phys.*, 2012, **137**, 064112.

36 T. Pugh, N. F. Chilton and R. A. Layfield, A low-symmetry dysprosium metallocene single-molecule magnet with a high anisotropy barrier, *Angew. Chem. Int. Ed.*, 2016, **55**, 11082–11085.

37 S. K. Gupta, T. Rajeshkumar, G. Rajaraman and R. Murugavel, An air-stable Dy(iii) single-ion magnet with high anisotropy barrier and blocking temperature, *Chem. Sci.*, 2016, **7**, 5181–5191.

38 S.-S. Liu, J. W. Ziller, Y.-Q. Zhang, B.-W. Wang, W. J. Evans and S. Gao, A half-sandwich organometallic single-ion magnet with hexamethylbenzene coordinated to the Dy(iii) ion, *Chem Commun*, 2014, **50**, 11418–11420.

39 I. F. Díaz-Ortega, J. M. Herrera, S. Dey, H. Nojiri, G. Rajaraman and E. Colacio, The effect of the electronic structure and flexibility of the counteranions on magnetization relaxation in $[Dy(L)_2(H_2O)_5]^{3+}$ (L = phosphine oxide derivative) pentagonal bipyramidal SIMs, *Inorg. Chem. Front.*, 2020, **7**, 689–699.

40 D. Pinkowicz, H. I. Southerland, C. Avendaño, A. Prosvirin, C. Sanders, W. Wernsdorfer, K. S. Pedersen, J. Dreiser, R. Clérac, J. Nehrkorn, G. G. Simeoni, A. Schnegg, K. Holldack and K. R. Dunbar, Cyanide single-molecule magnets exhibiting solvent dependent reversible "on" and "off" exchange bias behaviour, *J. Am. Chem. Soc.*, 2015, **137**, 14406–14422.

41 S. M. J. Aubin, Z. Sun, L. Pardi, J. Krzystek, K. Folting, L.-C. Brunel, A. L. Rheingold, G. Christou and D. N. Hendrickson, Reduced anionic Mn_{12} molecules with half-integer ground states as single-molecule magnets, *Inorg. Chem.*, 1999, **38**, 5329–5340.

42 J. Liu, Y.-C. Chen, J.-L. Liu, V. Vieru, L. Ungur, J.-H. Jia, L. F. Chibotaru, Y. Lan, W. Wernsdorfer, S. Gao, X.-M. Chen and M.-L. Tong, A stable pentagonal bipyramidal Dy(III) single-ion magnet with a record magnetization reversal barrier over 1000 K, *J. Am. Chem. Soc.*, 2016, **138**, 5441–5450.